A 0.14-mm² 1.4-mW 59.4-dB-SFDR 2.4-GHz ZigBee/WPAN Receiver Exploiting a "Split-LNTA + 50% LO" Topology in 65-nm CMOS

Zhicheng Lin, *Student Member, IEEE*, Pui-In Mak, *Senior Member, IEEE*, and Rui P. Martins, *Fellow, IEEE*

Abstract—A compact low-power 2.4-GHz ZigBee/wireless personal area network receiver is reported. It optimizes passive pregain with an inverter-based split low-noise transconductance amplifier (split-LNTA) to avoid the RF balun and its associated insertion loss, while enabling isolated in-phase (I)/quadrature (Q) passive mixing. The latter essentially saves power as a 50%-duty-cycle local oscillator (50% LO) can be generated more efficiently than its 25% counterpart. Specifically, a 2.4-GHz *LC* voltage-controlled oscillator (VCO) followed by an input-impedance-boosted Type-II *RC-CR* network produces the desired 50% four-phase LO with optimized power, I/Q accuracy, and phase noise. We also analytically compare the proposed "split-LNTA + 50% LO" architecture with the existing "single-LNTA + 25% LO," identifying their distinct features under current- and voltage-mode operations. The receiver fabricated in 65-nm CMOS exhibits 32-dB voltage gain, 8.8-dB noise figure (NF) and −7-dBm out-band input-referred third-order intercept point that correspond to 59.4-dB spurious-free dynamic range. The VCO measures −111.4-dBc phase noise at 3.5-MHz offset. The achieved power (1.4 mW) and area (0.14 mm²) efficiencies are favorably comparable with the state-of-the-art.

Index Terms—CMOS, local oscillator (LO), low-noise transconductance amplifier (LNTA), passive mixer, *RC-CR* network, receiver, RF, transimpedance amplifier (TIA), voltage-controlled oscillator (VCO).

I. INTRODUCTION

THE proliferation of short-range wireless applications for Internet of Things and personal healthcare calls for ultra-low power and cost CMOS radios [1]. Ultra-low voltage (ULV) designs have been one of the key directions to approach a better power efficiency [2]–[5]. Regrettably, an ULV supply will limit the voltage swing, and device's f_T and overdrives, deteriorating the spurious-free dynamic range (SFDR) while

Z. Lin and P.-I. Mak are with the State-Key Laboratory of Analog and Mixed-Signal VLSI and FST-ECE, University of Macau, Macao, China. (e-mail: pimak@umac.mo).
R. P. Martins is with the State-Key Laboratory of Analog and Mixed-Signal VLSI and FST-ECE, University of Macau, Macao, China, and also with the Instituto Superior Técnico, Universidade de Lisboa, Lisbon, Portugal (e-mail: rmartins@umac.mo).

Color versions of one or more of the figures in this paper are available online at http://ieeexplore.ieee.org.

Digital Object Identifier 10.1109/TMTT.2014.2324531

necessitating area-hungry inductors (or transformers) to assist the bias and tune out the parasitic capacitances. This paper describes the design and implementation of a compact, low-power, and high-SFDR receiver suitable for ZigBee or wireless personal area network (WPAN) applications. The research background can be introduced as follows.

Four potential receiver architectures are shown in Fig. 1. The first [see Fig. 1(a)] employs a single low-noise transconductance amplifier (single-LNTA) followed by two passive in-phase (I) and quadrature (Q) mixers and transimpedance amplifiers (TIAs). If a 50%-duty-cycle local oscillator (50% LO) is applied, this topology can suffer from image current circulation between the I and Q paths, inducing I/Q crosstalk, unequal high-side, and low-side gains, input-referred second-order intercept point (IIP2) and input-referred third-order intercept point (IIP3) [6]. Lowering the LO duty cycle to 25% [see Fig. 1(b)] can alleviate such issues [7] at the expense of extra sine-to-square LO buffers and logic operation. Another alternative is to add two signal buffers before the mixers [see Fig. 1(c)], but they must be linear enough (i.e., more power) to withstand the voltage gain of the low-noise amplifier (LNA) [8], [9]. The basis of our proposed solution [see Fig. 1(d)] is to split the LNTA into two, such that a single-ended RF input is maintained, while allowing isolated passive mixing that facilitates the use of a 50% LO for power savings.

This paper is organized as follows. Section II overviews the operating principle of the proposed "split-LNTA + 50% LO" receiver. An analytical comparison of it with the existing "single-LNTA + 25% LO" architecture is given in Section III. In Section IV, a number of techniques are proposed, including: 1) a low-power voltage-mode TIA to enhance the out-channel linearity both at RF and baseband (BB); 2) a mixed-supply (V_{DD}) design approach [10] to alleviate the design tradeoffs in RF LNTA (power, gain, and noise) and BB TIA (power, linearity, and signal swing); 3) a low-power LO generation scheme that consists of an *LC* voltage-controlled oscillator (VCO), and an *input-impedance-boosted* Type-II *RC–CR* network. They optimize the VCO's output swing with the *LC* tank's quality factor, while offering adequate I/Q accuracy at low power. The measurement results are reported in Section V, and conclusions are drawn in Section VI.

II. PROPOSED "SPLIT-LNTA + 50% LO" RECEIVER

The split-LNTA (Fig. 2) is based on two self-biased inverter-based amplifiers (M_1, M_2, and R_F), which have no
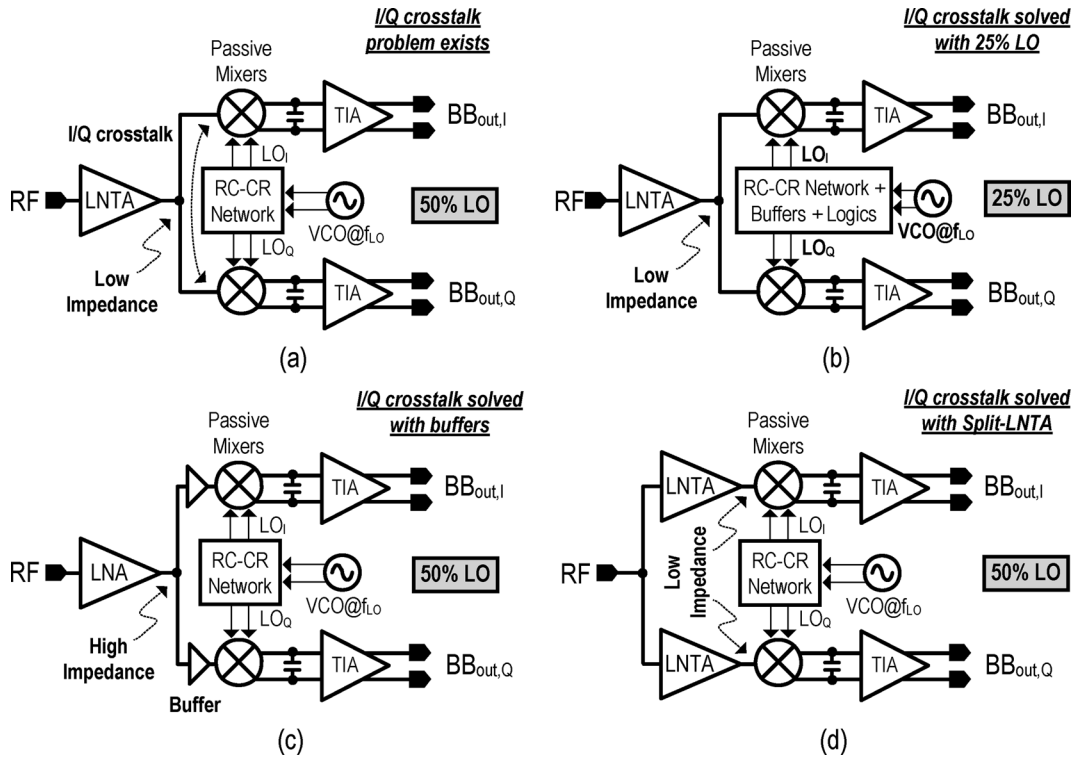
Fig. 1.   Four potential receiver architectures. (a) Single-LNTA + 50% LO. (b) Single-LNTA + 25% LO. (c) Single-LNA + 50% LO + signal buffers. (d) Split-LNTA + 50% LO (proposed).
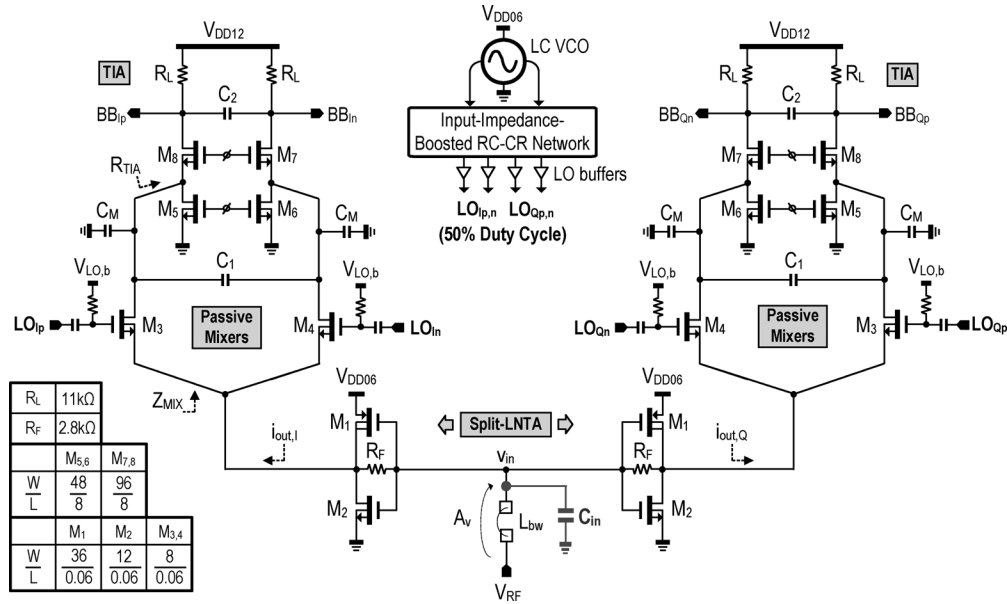

Fig. 2.   Schematic of the proposed receiver exploiting passive pre-gain, split-LNTA, passive mixers, 50% LO and common-gate TIAs.

inner parasitic pole. They also can take the speed advantage of fine linewidth CMOS to lower the device overdrive voltages, featuring a high g_m-to-I_d efficiency at low V_{DD} (V_{DD06} = 0.6 V). Its single-ended RF input avoids the RF balun and its associated insertion loss. In front of the split-LNTA, a proper co-design between the RF input capacitance (C_{in}) and bondwire (L_{bw}) facilitates the input impedance matching, while offering a passive pre-gain (A_v) decisively important to the noise figure (NF) and power efficiency. The two LNTAs convert the RF signal (v_{in}) into two equal currents $i_{out,I}$ and $i_{out,Q}$ for the I and Q channels, respectively. To

avoid the parasitics and area impact from ac coupling, $i_{out,I}$ and $i_{out,Q}$ are directly dc-coupled to the passive mixers (M_3 and M_4). As long as the dc current passing through M_3 and M_4 is kept small, the $1/f$ noise induced by the mixers can be minimized [11]. This aim can be achieved by matching the output common-mode level of the LNTA to that of the BB TIA.

The 50% four-phase LO ($LO_{Ip,n}$ and $LO_{Qp,n}$) is generated by a 2.4-GHz LC VCO followed by a new type-II RC–CR network, which features a capacitor divider at the input to boost the input impedance. When driving the LO to the mixers (M_3 and M_4), a proper dc level ($V_{LO,b}$) can optimize the switching
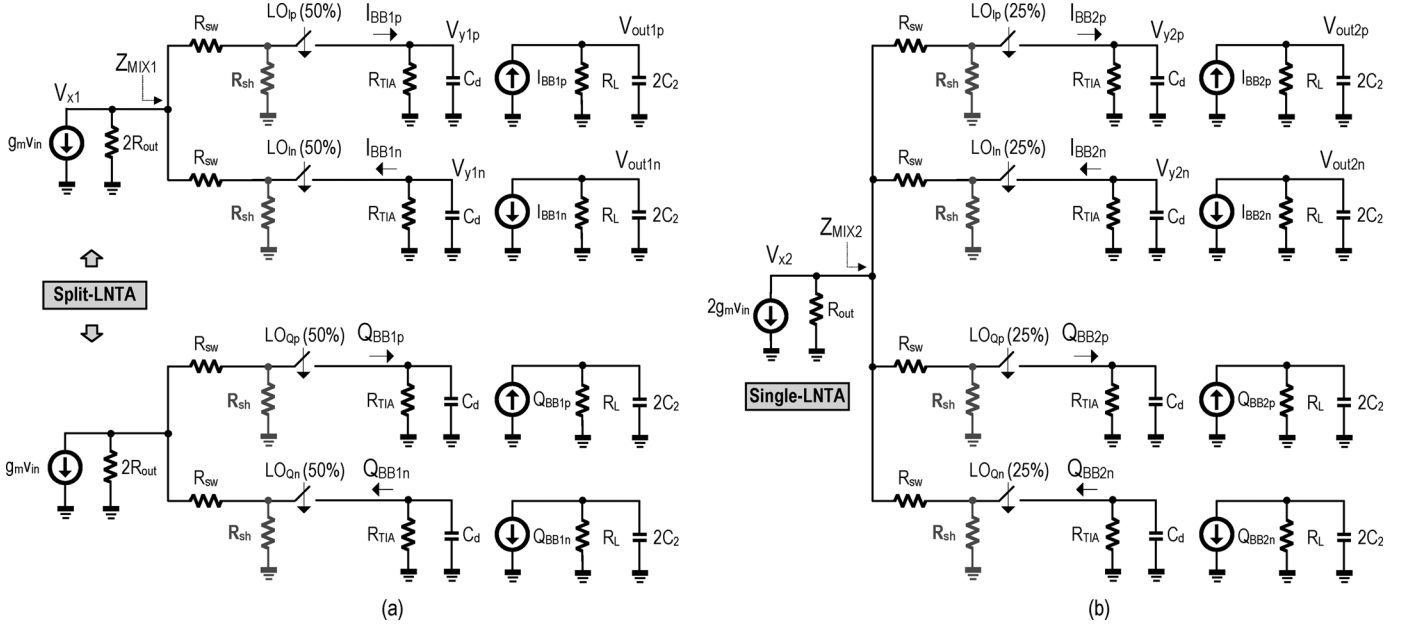
Fig. 3. Small-signal equivalent circuits. (a) Split-LNTA + 50% LO. (b) Single-LNTA + 25% LO.

time. The downconverted low-IF (2 MHz) signal is further amplified by a common-gate TIA (M_{5-8} and R_L), which uses a 1.2-V (V_{DD12}) supply to accommodate more signal swing and enhance linearity. Here, we assume a complex low-IF filter will follow the BB TIA, rendering the $1/f$ noise and IIP2 not significant and will not be further addressed. Due to the bidirectional transparency of passive mixers [7], [8], the BB capacitors (C_1 and C_M) can enhance the selectivity at both RF (the output of the LNTA) and BB, improving the out-band linearity. The grounded C_M also helps to suppress the common-mode RF feedthrough, which is limited by the bondwire inductance that appears in series with C_M under common-mode operation.

III. COMPARISON OF "SPLIT-LNTA + 50% LO" AND "SINGLE-LNTA + 25% LO" ARCHITECTURES

This section presents an analytical comparison of the two architectures: "split-LNTA + 50% LO" and "single-LNTA +25% LO." For brevity, "50% LO" and "25% LO" are exploited to represent them, respectively. Fig. 3(a) and (b) shows their simplified equivalent circuits. For a fair comparison, the two LNTAs in Fig. 3(a) are modeled as g_m (transconductance) and $2R_{out}$ (output resistance), whereas the single LNTA in Fig. 3(b) is modeled as $2g_m$ and R_{out}. These models are developed under the same approach described in [12]–[14], where the harmonic up-conversion in passive mixers is modeled as R_{sh}. The impedances looking into the 50%-LO and 25%-LO mixers are denoted as Z_{MIX1} and Z_{MIX2}, respectively. Each mixer features an on-resistance of R_{sw}. R_{TIA} is the input resistance of the TIA. The single-ended differential mode capacitance is denoted as C_d ($= C_M + 2C_1$).

A. Gain

For Fig. 3(a), we summarize in (1)–(5) the derived expressions of both Z_{MIX1} and the voltage gain (A_{Vx1}) at V_{x1} at the LO + IF frequency ($\omega_{LO} + \omega_{IF}$); the BB output current (I_{BB1})

with respect to v_{in}; the voltage gain (A_{Vy1}) at $V_{y1p,n}$, and finally, the voltage gain (A_{Vout1}) at $V_{out1p,n}$,

$$Z_{MIX1}|@(\omega_{LO} + \omega_{IF}) \approx R_{sw} + \left(\frac{2Z_{BB}}{\pi^2} // R_{sh} \right) \quad (1)$$

where

$$Z_{BB} = \frac{1}{s(2C_1 + C_M)} // R_{TIA}$$

$$R_{sh} \approx \frac{2}{3} (2R_{out} + R_{sw})$$

$$A_{Vx1}@(\omega_{LO} + \omega_{IF}) \approx g_m (2R_{out} // Z_{MIX1}) \quad (2)$$

$$\frac{I_{BB1}}{v_{in}}@DC = \frac{I_{BB1p} - I_{BB1n}}{v_{in}}$$

$$\approx g_m \frac{2R_{out}}{R_{TIA} + 2(2R_{out} + R_{sw})} \frac{4}{\pi} = G_{m1} \quad (3)$$

$$A_{Vy1}@DC = A_{Vy1p} - A_{Vy1n} \approx G_{m1}R_{TIA} \quad (4)$$

$$A_{Vout1}@DC = A_{Vout1p} - A_{Vout1n} \approx G_{m1}R_L. \quad (5)$$

Similarly, for Fig. 3(b), we have (6)–(10), the derived expressions of both Z_{MIX2} and the voltage gain (A_{Vx2}) at V_{x2} at the LO + IF frequency ($\omega_{LO} + \omega_{IF}$); the BB output current (I_{BB2}) with respect to v_{in}; the voltage gain (A_{Vy2}) at $V_{y2p,n}$, and finally, the voltage gain (A_{Vout2}) at $V_{out2p,n}$,

$$Z_{MIX2}|@(\omega_{LO} + \omega_{IF}) \approx R_{sw} + \left(\frac{2Z_{BB}}{\pi^2} // R_{sh} \right) \quad (6)$$

where

$$Z_{BB} = \frac{1}{s(2C_1 + C_M)} // R_{TIA}$$

$$R_{sh} \approx 4 (R_{out} + R_{sw})$$

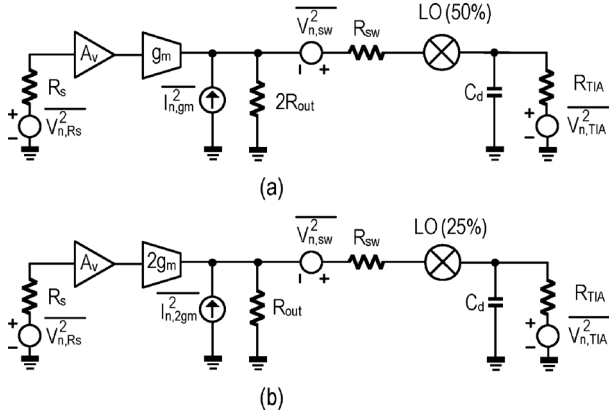$$A_{Vx2}@(\omega_{LO} + \omega_{IF}) \approx 2g_m (R_{out} // Z_{MIX2}) \quad (7)$$

Fig. 4. Equivalent LTI noise model with pre-gain for: (a) 50% LO [see Fig. 3(a)] and (b) 25% LO [see Fig. 3(b)].

Fig. 5. Simulated NF_{DSB} and ΔNF against A_v for 50% LO and 25% LO.

$$\frac{I_{BB2}}{v_{in}} @DC = \frac{I_{BB2p} - I_{BB2n}}{v_{in}}$$

$$\approx 2g_m \frac{R_{out}}{R_{TIA} + 4(R_{out} + R_{sw})} \frac{4\sqrt{2}}{\pi}$$

$$= G_{m2} \qquad (8)$$

$$A_{Vy2} @DC = A_{Vy2p} - A_{Vy2n} \approx G_{m2}R_{TIA} \qquad (9)$$

$$A_{Vout2} @DC = A_{Vout2p} - A_{Vout2n} \approx G_{m2}R_L. \qquad (10)$$

Note that the output capacitance of the LNTA was neglected. In fact, the output capacitance of LNTA will induce C_{out} and $2C_{out}$ for the g_m and $2g_m$ LNTA stages, respectively. This will render the output impedance ratio at V_{x1} and V_{x2} slightly larger than 2. Besides, the parasitic capacitor will also affect R_{sh}. The proposed separated g_m stage imposes a smaller C_{out} and thus lowers the degradation of gain and NF than those predicted by (11) and (12). With proper sizing, one can achieve $R_{sw} \ll R_{out}$ and $R_{sw} \ll R_{TIA}$ and R_L, such that the gain difference between 25% LO and 50% LO at different RF and BB nodes can be estimated as

$$A_{Vx1,2} @\omega_{LO} = 20\log A_{Vx2} - 20\log A_{Vx1}$$

$$\approx 20\log \frac{2\left(R_{out}//\frac{2R_{TIA}}{\pi^2}//4R_{out}\right)}{2R_{out}//\frac{2R_{TIA}}{\pi^2}//\frac{4R_{out}}{3}}$$

$$= 6 \text{ dB}$$

$$\Delta A_{Vy1,2} @DC = 20\log A_{Vy2} - 20\log A_{Vy1}$$

$$= 20\log\left(\sqrt{2}\frac{R_{TIA} + 4R_{out} + 2R_{sw}}{R_{TIA} + 4R_{out} + 4R_{sw}}\right)$$

$$\approx 3 \text{ dB}$$

$$\Delta A_{Vout1,2} @DC = 20\log A_{Vout2} - 20\log A_{Vout1}$$

$$= 20\log\left(\sqrt{2}\frac{R_L + 4R_{out} + 2R_{sw}}{R_L + 4R_{out} + 4R_{sw}}\right)$$

$$\approx 3 \text{ dB}. \qquad (11)$$

From (11), the 25% LO should have a higher gain at both RF and BB nodes than the 50% LO. However, as analyzed in Section III-C, a higher gain at RF will penalize the IIP3, while a higher BB gain can be achieved easily by using a larger R_L. For the impact of these gain differences to NF, we analyze them next.
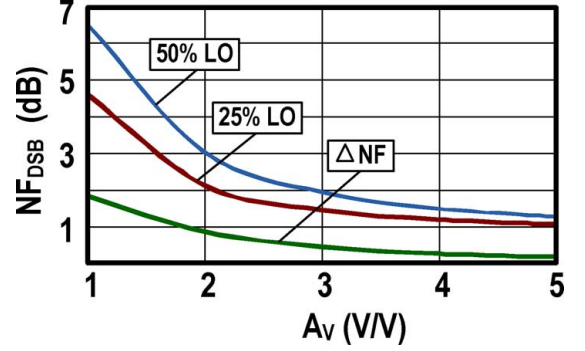
B. NF

The NF is analyzed according to the equivalent LTI noise model [12]–[14]. As shown in Fig. 4(a) and (b), the four noise sources are the thermal noises from $R_s(V_{n,Rs}^2 = 4kTR_s)$, LNTA($I_{n,g_m}^2 = 4kT\gamma_1 g_m$ or $I_{n,2g_m}^2 = 4kT\gamma_1 2g_m$), $R_{sw}(V_{n,sw}^2 = 4kTR_{sw})$ and the noise from the TIA is $V_{n,TIA}^2 \approx 4kT\gamma_2/g_{m\_TIA} \approx 4kT\gamma_2 R_{TIA}$, given that the output impedance of the mixer is sufficiently large. Here, g_{m_TIA} is the transconductance of the bias transistor for the TIA, while the noise from the CG device is degenerated. An accurate model of the TIA noise can be found elsewhere[11]. The noise of R_F is ignorable and the noise coupling between the I and Q paths under a 50% LO is minor (confirmed by simulations), easing the NF calculation of each path separately. The noise factor (F) can be found by dividing the total output noise by the portion contributed by R_s,

$$F = 1 + \frac{\gamma_1}{R_s A_v^2 G_m} + \frac{R_{sw}}{R_s A_v^2 G_m^2 R^2} + \frac{(R + R_{sw})^2}{R_s A_v^2 G_m^2 R^2 \beta \gamma_2 R_{TIA}}$$

$$+ \frac{a\gamma_1}{R_s A_v^2 G_m} + a + \frac{aR_{sw}}{R_s A_v^2 G_m^2 R^2} \qquad (12)$$

where $\beta = 2/\pi^2$ is the down-conversion scaling factor and a is the harmonic folding factor

$$a = \left(\frac{\pi^2}{4} - 1\right), \ G_m = g_m, \text{ and } R = 2R_{out} \text{ for Fig. 4(a)}$$

$$a = \left(\frac{\pi^2}{8} - 1\right), \ G_m = 2g_m, \text{ and } R = R_{out} \text{ for Fig. 4(b)}.$$

In (12), the second term is from the LNTA, the third term is from the mixer, and the fourth term is from the TIA. The rest of the terms are the noise folding from the odd harmonics of the LO for the LNTA, R_s and R_{SW}, respectively. The NF calculated from (12) for 50% LO is single sideband (SSB). For a double-sideband (DSB) NF, it is 3 dB less. Since the harmonic's power of the 50% LO is larger than that of the 25% LO, the folding terms of the 50% LO are also higher. From (12), one can plot the DSB NF of the 50% LO and 25% LO in Fig. 5 as a function of A_V, where $\Delta NF = NF_{50\%} - NF_{25\%}$, $R_{sw} = 50\ \Omega$, $\gamma_1 = \gamma_2 = 1$, $g_m = 9$ mS, $R_{out} = 200\ \Omega$, and $R_{TIA} = 2.5$ kΩ. It can be seen that ΔNF is reduced to 0.91 dB (0.51 dB) when A_V is just 2 V/V (3 V/V), which is easily achievable in practice. In fact, a moderated A_V can even eliminate the need of the LNTA (or LNA) [3]. However, when also considering the input matching and LO-to-RF isolation, both pre-gain and the LNTA should

be employed concurrently. The simulated LO-to-RF isolation is < -100 dBm. Due to the passive pre-gain, the IIP3 of the receiver is more demanding than the NF, promoting the use of a 50% LO. Together with its power advantage (i.e., lower VCO frequency and no divider), our proposed topology (i.e., pre-gain + split-LNTA + 50% LO) should ease the tradeoff between the NF, IIP3, area, and power.

C. IIP3

The third-order intermodulation (IM3) distortion is analyzed to assess the linearity. The aim is to find the in-band IIP3 of the receiver under 50% LO and 25% LO in response to two-tone excitation. Assuming that the nonlinearity of the receiver is dominated by the LNTA, its nonlinearity contributions are considered as follows:

  a) third-order LNTA nonlinearity due to input excitation $v_{\rm in}$ [$\alpha_2(I/V^3)$];
  b) third-order LNTA nonlinearity due to output excitation v_x [$\alpha_3(I/V^3)$].

Thus, $i_{\rm ds} = \alpha_1 v_{\rm in} + \alpha_2 v_{\rm in}^3 + \alpha_3 v_X^3$. If the coefficients α_1, α_2, and α_3 are assumed to be proportional to the device W/L.

For 50% LO, $\alpha_1 = g_m$, $\alpha_2 = g_{m3}$, $\alpha_3 = g_{o3}$.

For 25% LO, $\alpha_1 = 2g_m$, $\alpha_2 = 2g_{m3}$, $\alpha_3 = 2g_{o3}$.

g_{m3} and g_{03} are the third-order nonlinear transconductance and conductance, respectively. With a two-tone excitation of amplitude A and the first-order voltage gain and current gain given in (1)–(11), the IM3 output voltage for each of the nonlinear coefficients listed above can be written as

$$v_{o3\alpha2} = \frac{3}{4}g_{m3}A^3 I_{\rm BB1}R_L; \; v_{o3\alpha3} = \frac{3}{4}g_{o3}A_{Vx1}^3 A^3 I_{\rm BB1}R_L$$

for a 50% LO. Thus,

$$\mathrm{IM}_{3\_50\%} = \frac{v_{o3\alpha2} + v_{o3\alpha3}}{v_{01\alpha1}}$$
$$= \frac{\frac{3}{4}g_{m3}A^3 I_{\rm BB1}R_L + \frac{3}{4}g_{o3}A_{Vx1}^3 A^3 I_{\rm BB1}R_L}{Ag_m I_{\rm BB1}R_L}.$$

Let

$$\mathrm{IM}_{3\_50\%} = 1 \rightarrow \mathrm{IIP}_{3\_50\%} = \sqrt{\frac{4g_m}{3(g_{m3} + g_{o3}A_{Vx1}^3)}}. \quad (13)$$

Following the same procedure, the IIP3 for 25% LO can be derived as

$$\mathrm{IIP}_{3\_25\%} = \sqrt{\frac{4g_m}{3(g_{m3} + g_{o3}A_{Vx2}^3)}}. \quad (14)$$

Since $A_{Vx2} > A_{Vx1}$, we can find that, from (13) and (14), the LNTA's third-order nonlinearity term is larger for a 25% LO. Thus, the IIP3 of the 50% LO should be better than that of the 25% LO, benefiting the SFDR since both architectures will feature a similar NF after adding the pre-gain.

D. Current- and Voltage-Mode Operations

Both 25% LO and 50% LO architectures can be intensively designed for current- or voltage-mode operation. For a *high-performance* design like [7], [8], and [12], $R_{\rm TIA} \ll R_{\rm out}$ and

Mode	Gain	NF	In-Band IIP3	Power	Suitable for
Current Mode (Small $R_{\rm sw}$ & $R_{\rm TIA}$)	↗	↘	↗	↗	High Performance
Voltage Mode (Large $R_{\rm sw}$ & $R_{\rm TIA}$)	↘	↗	↘	↘	Ultra Low Power

$R_{\rm sw} \ll R_{\rm out}$ are preferred to keep the signals in the deep current mode. As such, (3) and (8) can be simplified as $G_{m1} = 2g_m/\pi$ and $G_{m2} = 2\sqrt{2}g_m/\pi$, respectively. Both of them are higher when compared to themselves in the voltage-mode operation. In terms of IIP3 and NF, the current mode is also preferable since $A_{Vx1} \approx g_m(R_{\rm sw} + (2/\pi^2)R_{\rm TIA})$ and $A_{Vx2} \approx 2g_m(R_{\rm sw} + (2/\pi^2)R_{\rm TIA})$ will be lower, and the noise due to the folding term and TIA will be also smaller, as noted in (12).

Nevertheless, the current-mode operation also brings up two sizing constraints being less attractive for *low-power* design, which are: 1) a low $R_{\rm sw}$ entails a large device W/L and a higher overdrive voltage for the mixers; both calling for a larger power budget in the LO path and 2) a low $R_{\rm TIA}$ implies that the TIA has to draw a large bias current. For example, if a low $R_{\rm TIA}$ of 50 Ω is required from the 1.2-V TIA (a common-gate amplifier), its bias current is as high as $I_{\rm bias} = 2$ mA for a typical overdrive voltage of 200 mV. Thus, for *ultra-low-power* applications like Zigbee/WPAN that has relaxed NF and linearity requirements, higher $R_{\rm sw}$ and $R_{\rm TIA}$ are preferable to operate the receiver *more* on the voltage mode. A summary of performance differences in current- and voltage-mode operations is given in Table I.

IV. CIRCUIT TECHNIQUES

A. Impedance Up-Conversion Matching

From Section III, we expect a passive pre-gain A_v of 2–3 V/V. As shown in Fig. 6(a), A_v can be derived under $R_{\rm in} = R_s$,

$$\frac{V_{\rm out}^2}{2R_{\rm out}} = \frac{V_s^2}{8R_s}, \; V_{\rm out} = V_{\rm in}A_v, \; V_{\rm in} = 0.5V_s \Rightarrow A_v = \sqrt{\frac{R_{\rm out}}{R_{\rm in}}}.$$

Thus, an *up-conversion* matching network is entailed to ensure $A_v > 1$. A convenient way to achieve it is to use $L_{\rm bw}$ to resonant with $C_{\rm in}$. The schematic is shown in Fig. 6(b). The parallel connection of $C_{\rm in}$ and $R_{\rm out}$ can be transformed into a series connection of $C_{\rm ser}$ and $R_{\rm ser}$, as shown in Fig. 6(c). At $L_{\rm bw}C_{\rm ser}$ resonance, and with $R_{\rm ser} = R_s$ and $i = V_s/2R_{\rm ser}$, we have

$$V_{\rm out} = V_{R_{\rm ser}} + V_{C_{\rm ser}} = \frac{V_S}{2}\left(1 - j\frac{Q_C}{2}\right)$$

where

$$V_{R_{\rm ser}} = -j\frac{Q_C V_s}{2}sC_{\rm ser}R_{\rm ser} = \frac{V_s}{2}$$

$$V_{C_{\rm ser}} = \frac{1}{j\omega_0 C_{\rm ser}}\frac{V_s}{2R_{\rm ser}} = -j\frac{Q_C}{2}V_s,$$

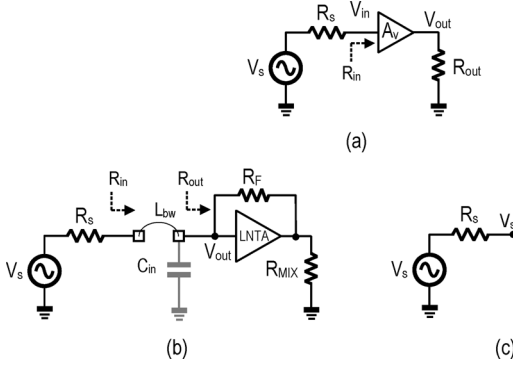$$\omega_0 = \frac{1}{\sqrt{L_{\rm bw}C_{\rm ser}}} \text{ and } Q_C = \frac{\sqrt{\frac{L_{\rm bw}}{C_{\rm ser}}}}{R_{\rm ser}}.$$

Fig. 6. Input impedance matching. (a) A_v converts R_{out} to R_{in} to match with R_s. (b) $L_{\text{bw}} C_{\text{in}}$ as an impedance conversion network and its (c) narrowband equivalent circuit.

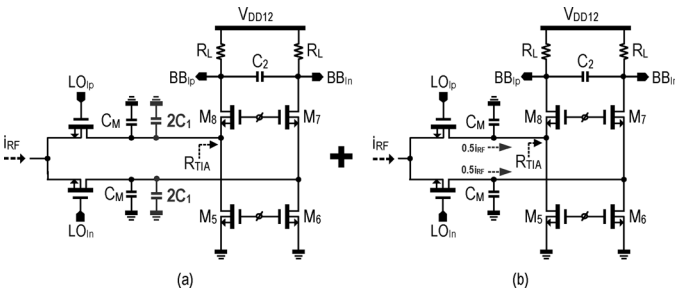Fig. 8. Out-band IIP3 can be improved by allowing more total capacitance of $C_M + 2C_1$.

Fig. 7. Equivalent circuits of the mixer-TIA interface for the: (a) differential low-IF signal and (b) common-mode RF feedthrough.

Fig. 9. On-resistance of the mixer switches represents a tradeoff among the LO-path's power, out-band IIP3, and NF.

Interestingly, such a voltage boosting factor $\sqrt{1 + Q_c^2/4}$ is larger than the conventional inductively degenerated LNA, which is only $Q_C/2$. In fact, when the capacitance of the printed circuit board (PCB) trace is accounted, the Q of the matching network will be higher, easing the impedance matching.

B. Mixer-TIA Interface Biased for Impedance Transfer Filtering

For the employed single-balanced passive mixers, the RF-to-IF feedthrough has to be addressed. Based on Fig. 7, we can calculate the currents i_{M7} and i_{M8} with respect to the RF current i_{RF} as given by

$$i_{M7} = \frac{i_{\text{RF}}}{2}[1 - \text{sign}\,(\cos \omega_{\text{LO}}t)] \tag{15}$$

$$i_{M8} = \frac{i_{\text{RF}}}{2}[1 + \text{sign}\,(\cos \omega_{\text{LO}}t)]. \tag{16}$$

They imply that the currents can be decomposed into the differential mode [see Fig. 7(a)] with an amplitude of $2i_{\text{RF}}/\pi$ at BB, and into the common mode [see Fig. 7(b)] with an amplitude of $0.5i_{\text{RF}}$ at RF. To suppress the latter, C_M was added to create a low-pass pole ($C_M//R_{\text{TIA}}$). For the differential IF signal, the pole is located at $(C_M + 2C_1)//R_{\text{TIA}}$, which suppresses the out-of-channel interferers before they enter the TIA. As such, the TIA can be biased under a very small bias current. The resultant high input impedance of the TIA, indeed, benefits both BB and RF filtering because of the bidirectional impedance-translation property of the passive mixers [7], [8]. Fig. 8 shows the simulated out-band IIP3, which is subject to the allowed total
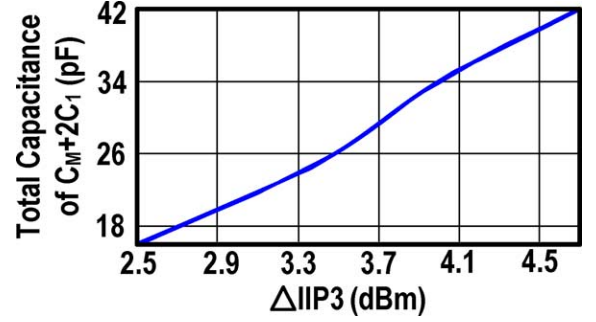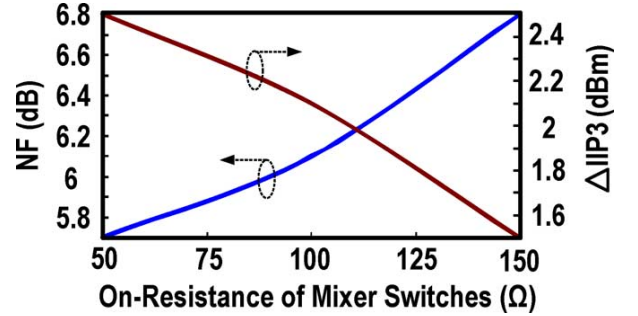
capacitance of $C_M + 2C_1$. For instance, when $C_M + 2C_1$ is increased from 16 to 42 pF, the out-band IIP3 raises from $+2.5$ to $+4.7$ dBm at the expense of the die area. For the on-resistance of the mixer switches (R_{sw}), it involves a tradeoff of the LO path's power to the out-band IIP3 and NF. As shown in Fig. 9, if R_{sw} is increased from 50 to 150 Ω for power savings, the NF and out-band IIP3 will be penalized by ~ 1 dB.

C. RC–CR Network and VCO Co-Design

The *LC* VCO [see Fig. 10(a)] employs a complementary NMOS–PMOS (M_{1-4}) negative transconductor. For power savings, M_1 and M_2 are based on ac-coupled gate bias ($V_{\text{vco},b}$) to lower the supply to 0.6 V. Here, we implement a capacitive divider (C_{M1} and C_{M2}) to boost the input impedance of its subsequent two-stage *RC–CR* network [see Fig. 10(b)]. The optimization details are presented next.

The *RC–CR* network is excellent for low-power and narrowband I/Q generation. With a Type-II architecture, both phase balancing and insertion loss can be better optimized than its Type-I counterpart [15]. For instance, the simulated insertion loss of a two-stage Type-II *RC–CR* network is roughly 2 dB, as shown in Fig. 11, which will be raised to 4–5 dB if a Type-I topology is applied (not shown). For low-power LO buffering, the amplitude balancing is critical because its imbalance will lead to inconsistent zero-crossing points, resulting in AM to duty-cycle distortion. Fig. 12 (V_{RC1-4}) and Fig. 13 ($\text{LO}_{Ip,n}$ and $\text{LO}_{Qp,n}$) are the simulated transient waveforms, showing the consistent duty cycle and zero-crossing points achieved in the proposed design.

For an *RC–CR* network operated at 2.4 GHz, if we select $R_{N1} = 1$ kΩ, C_{N1} is just 66 fF, which benefits the area, VCO
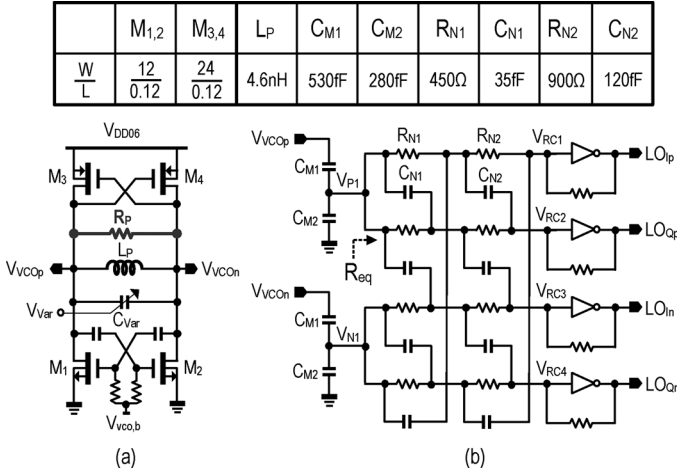
	$M_{1,2}$	$M_{3,4}$	L_P	C_{M1}	C_{M2}	R_{N1}	C_{N1}	R_{N2}	C_{N2}
$\frac{W}{L}$	$\frac{12}{0.12}$	$\frac{24}{0.12}$	4.6nH	530fF	280fF	450Ω	35fF	900Ω	120fF

Fig. 10. (a) *LC* VCO and (b) proposed input-impedance-boosted two-stage Type-II *RC–CR* network for four-phase 50% LO generation.
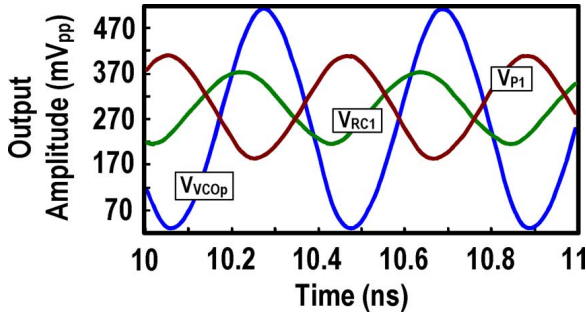

Fig. 11. Simulated time-domain signals at the output of the VCO (V_{vcop}), capacitor divider (V_{p1}), and the *RC–CR* network (V_{RC1}).
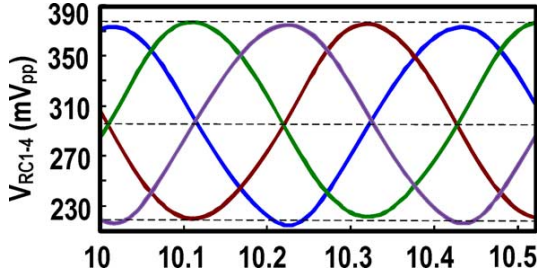

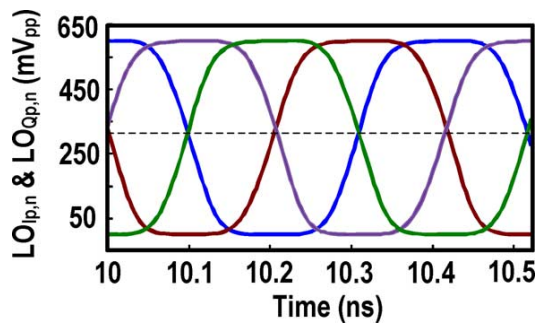Fig. 12. Simulated time-domain signals at V_{RC1-4}.

Fig. 13. Simulated time-domain signals at $\text{LO}_{Ip,n}$ and LO_{Qp-n}.

tuning range, and phase noise, but the I/Q accuracy over PVT variations should be considered [16]

$$\frac{\sigma \, (\text{Image Out})}{\text{Desired Out}} = 0.25 \sqrt{\left(\frac{\sigma_R}{R}\right)^2 + \left(\frac{\sigma_C}{C}\right)^2}. \qquad (17)$$
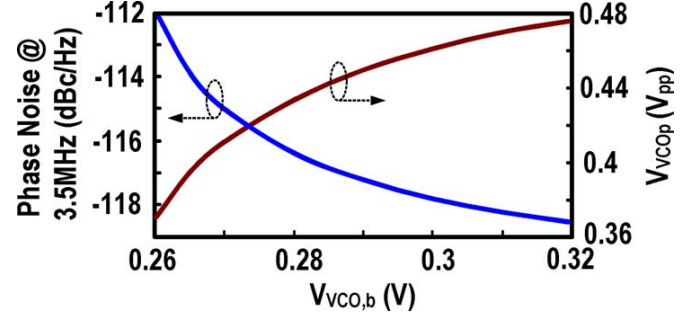

Fig. 14. Tradeoff between VCO output amplitude and phase noise with respect to $V_{\text{vco},b}$.
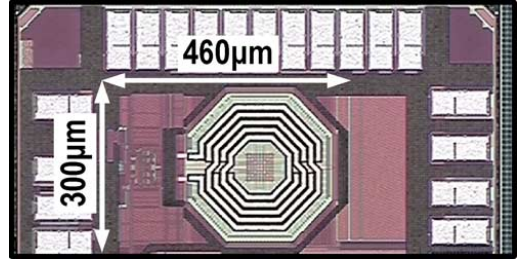

Fig. 15. Chip micrograph of the fabricated receiver.

Since ZigBee/WPAN applications call for a low image-rejection ratio (IRR) of 20–30 dB [17], according to (17), the matching of the resistors (σ_R) and capacitors (σ_C) can be relaxed to 2.93% for a 30-dB IRR (3σ). The sizes of $C_{N1,2}$ and $R_{N1,2}$ are summarized in Fig. 10. The poles from $C_{N1,2}$ and $R_{N1,2}$ are distributed around 2.4 GHz to cover the PVT variations. The impact of R_{N1} to the VCO can be analyzed as follows.

When the VCO's inductor is 4 nH with a Q of 20 ($R_P \approx$ 1.2 kΩ), we have $R_{\text{tank}} \approx 0.5R_P//0.5R_{N1}$. Thus, directly connecting the *RC–CR* network to the VCO will limit the *LC* tank's Q_{tank} degrading the phase noise [18], [19]. To alleviate this, we boost up the equivalent input resistance of the *RC–CR* network (R_{eq}) by adding a capacitive divider (C_{M1} and C_{M2}). For the total tank capacitance C_{tank}, it can be approximated as

$$C_{\text{tank}} \approx 2C_{\text{Var}} + \frac{(C_{M2} + 2C_{N1})\,C_{M1}}{C_{M1} + C_{M2} + 2C_{N1}}. \qquad (18)$$

By defining an input-impedance boosting factor n,

$$n = \frac{C_{M1}}{C_{M1} + C_{M2} + 2C_{N1}} \qquad (19)$$

we have

$$V_{P1} \approx nV_{\text{VCO}p}. \qquad (20)$$

It means that the signal swing (V_{P1}) delivered to the *RC–CR* network are in tradeoff with n. Handily, in our VCO, sweeping $V_{\text{vco},b}$ can track the phase noise with the output swing (Fig. 14). Given a bias current and a phase-noise target, R_{tank} can be set from $V_{\text{VCO}p} \approx 2I_{\text{bias}}R_{\text{tank}}$, and n can be set from (21) with a specific R_p and R_{eq},

$$R_{\text{tank}} \approx \frac{R_{\text{eq}}}{n} \parallel \frac{R_P}{2}. \qquad (21)$$

In this work, $n = 0.6$ is selected to balance the output swing with C_{tank} and the total tank resistance (R_{tank}).
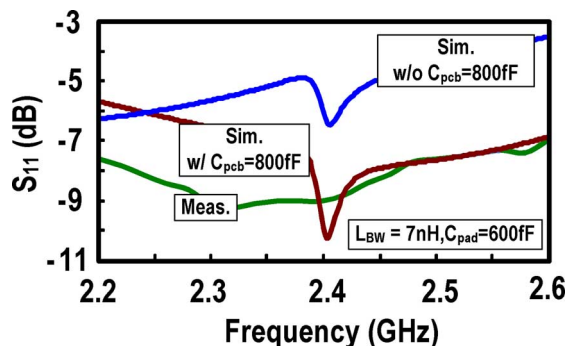
Fig. 16.   Measured S_{11}, and simulated S_{11} with and without C_{pcb}.
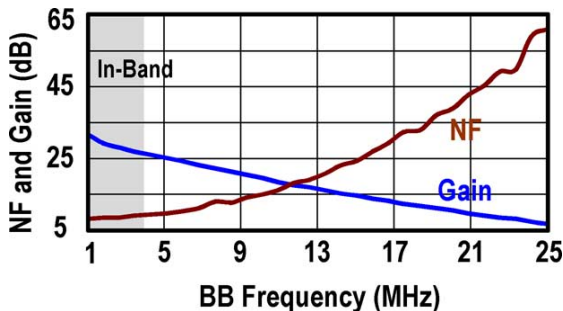

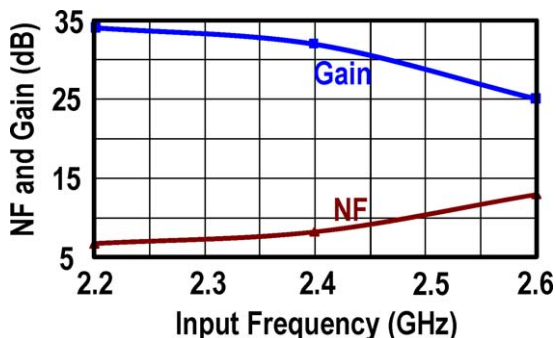Fig. 17.   Measured receiver gain and NF versus BB frequency.

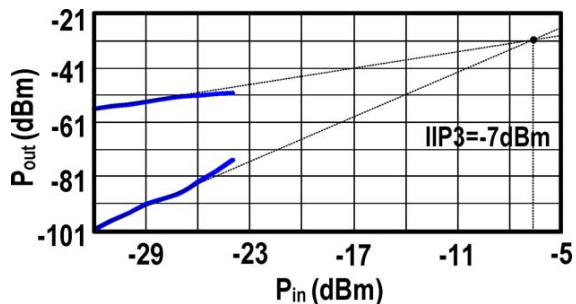Fig. 18.   Measured receiver gain and NF versus input signal frequency.

Fig. 19.   Measured out-of-band IIP3.

Fig. 20.   Measured VCO turning range.

Fig. 21.   Measured VCO phase noise at 2.4 GHz.
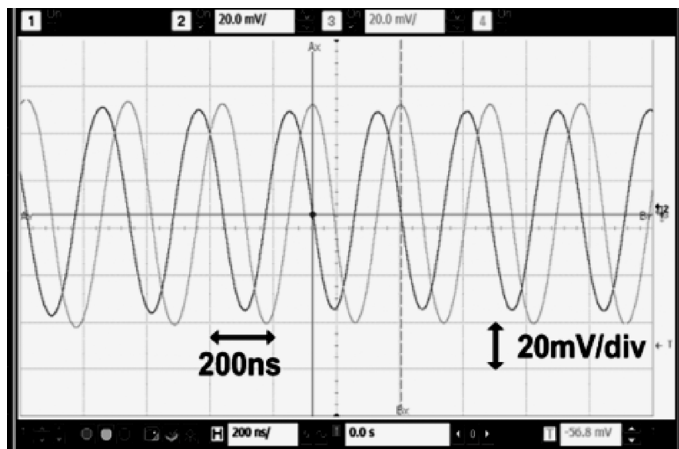
Fig. 22.   Measured I/Q BB transient outputs.

V. EXPERIMENTAL RESULTS

The receiver (Fig. 15) fabricated in 65-nm CMOS occupies an active area of 0.14 mm^2 and is encapsulated in a 44-pin CQFP package for PCB-based measurements. The estimated bondwire inductance is $\sim$ 7 nH for the provided package (13.5 × 13.5 mm). Fig. 16 shows that the measured S_{11} is -8 dB within 2.24–2.46 GHz (for a different package, an external inductor or capacitor can be added to optimize S_{11}). The simulation results with and without considering the PCB trace capacitances
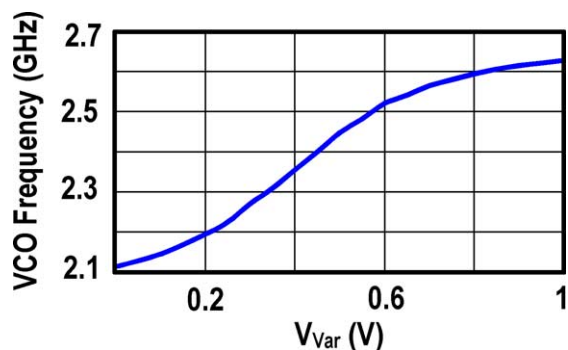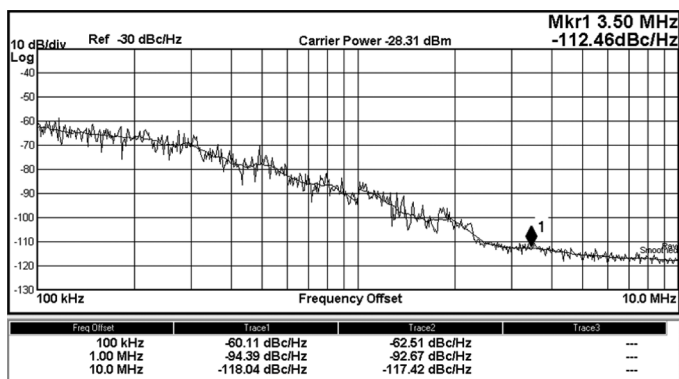
are also given. The measured voltage gain is 32.8–28.2 dB and the DSB NF is between 8.6–9 dB for an IF spanning from 1 to 3 MHz, as shown in Fig. 17. We also measured the gain and NF from 2.2 to 2.6 GHz (Fig. 18).

For a narrowband receiver, the linearity is mainly justified by the out-channel linearity tests. According to the case given in [17] and [20], two tones are applied at $[f_{\mathrm{LO}} + 10$ MHz, $f_{\mathrm{LO}} + 22$ MHz$]$ with a power level sweeping from -24 to -32 dBm. Due to the RF and BB filtering associated with the bidirectional property of passive mixers, the out-band IIP3 (Fig. 19) achieves -7 dBm and the $P_{1\ \mathrm{dB}}$ is -26 dBm.

For the VCO, it measures 21% tuning range from 2.623 to 2.113 GHz, as shown in Fig. 20. At 3.5-MHz offset, the phase noise (Fig. 21) is -112.46 dBc/Hz, fulfilling the specification

TABLE II
PERFORMANCE SUMMARY AND BENCHMARK WITH THE STATE-OF-THE-ART

Parameters	JSSC'08 [21]	JSSC'10 [22]	JSSC'10 [17]	TCAS-I'10 [24]	TMTT'11 [23]	TMTT'11 [26]	TMTT'06 [27]	ISSCC'13 [5]	ISSCC'13 [25]	This Work
Gain (dB)	35	67	75	24.5	51	22.5	30	83	55	**32**
DSB NF (dB)	7.5	16	9	16.5 (SSB)	3.2	7 (SSB)	7.3 (SSB)	6.1	9	**8.8**
Out-Band IIP3 (dBm)	-10	-10.5	-12.5	-19 (in-band data)	-32 (in-band data)	-21.5 (in-band data)	-8	-21.5	-6	**-7**
SFDR (dB)	58.3	52.3	55.5	38.3	36.5	51	59.8	51.6	60	**59.4**
VCO Phase Noise (dBc/√Hz)	N/A	-127 @ 3 MHz	-116 @3.5 MHz	N/A	N/A	N/A	N/A	-112 @ 1 MHz	-115 @ 3.5 MHz	**-111.4 @ 3.5 MHz**
Power (mW)	5.4 (w/o VCO)	32.5 (w/ VCO)	3.6 (w/ VCO)	2.52 (w/o VCO)	8.1 (w/o VCO)	1.06 (w/o VCO)	1.8 (w/o VCO)	1.6 (w/ VCO)	2.7 (w/ VCO)	**1.4 ᵇ (w/ VCO)**
No. of Inductor or Transformer	2	3	1	3	5	3	2	4	2	**1**
Die Area (mm²)	0.23 (w/o VCO)	2.88 (w/ VCO)	0.35 (w/ VCO)	N/A	1.27 (w/o VCO)	1.1 (w/o VCO)	2.07 ᵃ (w/o VCO)	2.5 ᵃ (w/ VCO)	0.26 ᵃ (w/ VCO)	**0.14 (w/ VCO)**
Supply (V)	1.35	0.6	1.2	1.8	1.8	1.2	1.8	0.3	0.6/1.2	**0.6/1.2**
CMOS Tech.	90 nm	90 nm	90 nm	0.18 μm	0.18 μm	0.18 μm	0.18 μm	65 nm	65 nm	**65 nm**

a: Include more BB gain stages and filters   b: The power breakdown is LNTA: 0.4 mW, TIA: 0.18 mW and VCO + Buffer: 0.82 mW

(−102 dBc/Hz [17], [20]) with an adequate margin. From frequency 100 kHz to 1 MHz, the result fits the $1/f^3$ slope, and from 1 to 10 MHz, it starts to be saturated, primarily limited by the small output amplitude (−28.31 dBm) of the test buffer.

Based on transient measurements, the I/Q BB differential outputs (Fig. 22) has ∼ 0.72-dB gain mismatch and 2° phase mismatch, corresponding to an IRR of ∼ 25 dB.

The performance summary and benchmark are given in Table II. This work succeeds in achieving the highest power and area efficiencies via proposing a mixed-V_{DD} topology co-optimized with a number of circuit techniques. Only one on-chip inductor is entailed in the VCO. The achieved NF and out-band IIP3 correspond to a competitive SFDR of 59.4 dB according to [17], [19]

$$\text{SFDR} = \frac{2(P_{\text{IIP3}} + 174 \text{ dBm} - \text{NF} - 10\log B)}{3} - \text{SNR}_{\min}$$
(22)

where $\text{SNR}_{\min} = 4$ dB is the minimum signal-to-noise ratio required by the application, and $B = 2$ MHz is the channel bandwidth. As presented in Figs. 8 and 9, the SFDR can be further optimized by allowing more budgets in area (bigger $C_M + 2C_1$) and/or power (smaller on-resistance of the mixer switches), being a design-friendly architecture easily adaptable to different specifications.

VI. CONCLUSIONS

A mixed-V_{DD} 2.4-GHz ZigBee/WPAN receiver measured state-of-the-art performances has been described. It features passive pre-gain, a split-LNTA, a high-input-impedance BB TIA, and a low-power 50% LO generation scheme. They together lead to improved power and area efficiencies, as well as a high SFDR while eliminating the need of a RF balun. These beneficial features render this work a superior receiver candidate for cost and power reduction of ZigBee/WPAN radios in nanoscale CMOS.

REFERENCES

[1] P. Choi *et al.*, "An experimental coin-sized radio for extremely low-power WPAN (IEEE 802.15.4) application at 2.4 GHz," *IEEE J. Solid-State Circuits*, vol. 38, no. 12, pp. 2258–2268, Dec. 2003.

[2] C.-H. Li, Y.-L. Liu, and C.-N. Kuo, "A 0.6-V 0.33-mW 5.5-GHz receiver front-end using resonator coupling technique," *IEEE Trans. Microw. Theory Techn.*, vol. 59, no. 6, pp. 1629–1638, Jun. 2011.

[3] B. W. Cook *et al.*, "Low-power, 2.4-GHz transceiver with passive RX front-end and 400-mV supply," *IEEE J. Solid-State Circuits*, vol. 41, no. 12, pp. 2767–2775, Dec. 2006.

[4] A. C. Herberg *et al.*, "A 250-mV, 352-μW GPS receiver RF front-end in 130-nm CMOS," *IEEE J. Solid-State Circuits*, vol. 46, no. 4, pp. 938–949, Apr. 2011.

[5] F. Zhang *et al.*, "A 1.6 mW 300 mV-supply 2.4 GHz receiver with −94 dBm sensitivity for energy-harvesting applications," in *Int. Solid-State Circuits Conf. Tech. Dig.*, Feb. 2013, pp. 456–457.

[6] A. Mirzaei *et al.*, "Analysis and optimization of current-driven passive mixers in narrowband direct-conversion receivers," *IEEE J. Solid-State Circuits*, vol. 44, no. 10, pp. 2678–2688, Oct. 2009.

[7] A. Mirzaei *et al.*, "Analysis and optimization of direct-conversion receivers with 25% duty-cycle current-driven passive mixers," *IEEE Trans. Circuits Syst. I, Reg. Papers*, vol. 57, no. 9, pp. 2353–2366, Sep. 2010.

[8] A. Balankutty and P. R. Kinget, "An ultra-low voltage, low-noise, high linearity 900-MHz receiver with digitally calibrated in-band feed-forward interferer cancellation in 65-nm CMOS," *IEEE J. Solid-State Circuits*, vol. 46, no. 10, pp. 2268–2283, Oct. 2011.

[9] Y. Feng *et al.*, "Digitally assisted IIP2 calibration for CMOS direct-conversion receivers," *IEEE J. Solid-State Circuits*, vol. 46, no. 10, pp. 2253–2267, Oct. 2011.

[10] P.-I. Mak and R. P. Martins, "A 0.46-mm² 4-dB NF unified receiver front-end for fullband mobile TV in 65-nm CMOS," *IEEE J. Solid-State Circuits*, vol. 46, no. 9, pp. 1970–1984, Sep. 2011.

[11] N. Poobuapheun *et al.*, "A 1.5-V 0.7-2.5-GHz CMOS quadrature demodulator for multiband direct-conversion receivers," *IEEE J. Solid-State Circuits*, vol. 42, no. 8, pp. 1669–1677, Aug. 2007.

[12] C. Andrews and A. C. Molnar, "A passive mixer-first receiver with digitally controlled and widely tunable RF interface," *IEEE J. Solid-State Circuits*, vol. 45, no. 12, pp. 2696–2708, Dec. 2010.

[13] C. Andrews and A. C. Molnar, "Implications of passive mixer transparency for impedance matching and noise figure in passive mixer-first receivers," *IEEE Trans. Circuits Syst. I, Reg. Papers*, vol. 57, no. 12, pp. 3092–3103, Dec. 2010.

[14] A. Molnar and C. Andrews, "Impedance, filtering and noise in N-phase passive CMOS mixers," in *Proc. IEEE CICC*, Sep. 2012, pp. 1–8.

[15] J. Kaykovuori, K. Stadius, and J. Ryynanen, "Analysis and design of passive polyphase filters," *IEEE Trans. Circuits Syst. I, Reg. Papers*, vol. 55, no. 11, pp. 3023–3037, Nov. 2008.

[16] F. Behbahani *et al.*, "CMOS mixers and polyphase filters for large image rejection," *IEEE J. Solid-State Circuits*, vol. 36, no. 9, pp. 873–887, Sep. 2001.

[17] A. Liscidini, M. Tedeschi, and R. Castello, "Low-power quadrature receivers for ZigBee (IEEE 802.15.4) applications," *IEEE J. Solid-State Circuits*, vol. 45, no. 9, pp. 1710–1719, Sep. 2010.

[18] T. H. Lee, *The Design of CMOS Radio-Frequency Integrated Circuits*, 2nd ed. Cambridge, U.K.: Cambridge Univ. Press, 2004.

[19] B. Razavi, *RF Microelectronics*, 2nd ed. Hoboken, NJ, USA: Prentice-Hall, 2011.

[20] W. Kluge *et al.*, "A fully integrated 2.4-GHz IEEE 802.15.4-compliant transceiver for ZigBee™ applications," *IEEE J. Solid-State Circuits*, vol. 41, no. 12, pp. 2767–2775, Dec. 2006.

[21] M. Camus *et al.*, "A 5.4 mW/0.07 mm² 2.4 GHz front-end receiver in 90 nm CMOS for IEEE 802.15.4 WPAN stand," *IEEE J. Solid-State Circuits*, vol. 43, no. 6, pp. 1372–1383, Jun. 2008.

[22] A. Balankutty *et al.*, "A 0.6-V Zero-IF/Low-IF receiver with integrated fractional-N synthesizer for 2.4-GHz ISM-band applications," *IEEE J. Solid-State Circuits*, vol. 45, no. 3, pp. 538–553, Mar. 2010.

[23] J.-S. Syu, C. Meng, and C.-L. Wang, "2.4-GHz low-noise direct-conversion receiver with deep N-well vertical-NPN BJT operating near cutoff frequency," *IEEE Trans. Microw. Theory Techn.*, vol. 45, no. 3, pp. 538–553, Mar. 2010.

[24] J. Kaykovuori, K. Stadius, and J. Ryynanen, "An energy-aware CMOS receiver front end for low-power 2.4-GHz applications," *IEEE Trans. Circuits Syst. I, Reg. Papers*, vol. 57, no. 10, pp. 2675–2684, Oct. 2010.

[25] Z. Lin, P.-I. Mak, and R. P. Martins, "A 1.7 mW 0.22 mm² 2.4 GHz ZigBee RX exploiting a current-reuse blixer + hybrid filter topology in 65 nm CMOS," in *Int. Solid-State Circuits Conf. Tech. Dig.*, Feb. 2013, pp. 448–449.

[26] J. L. Gonzalez *et al.*, "A 16-kV HBM RF ESD protection codesign for a 1-mW CMOS direct conversion receiver operating in the 2.4-GHz ISM band," *IEEE Trans. Microw. Theory Techn.*, vol. 59, no. 9, pp. 2318–2330, Sep. 2011.

[27] T.-K. Nguyen *et al.*, "A low-power RF direct-conversion receiver/transmitter for 2.4-GHz-band IEEE 802.15.4 standard in 0.18 μm CMOS technology," *IEEE Trans. Microw. Theory Techn.*, vol. 54, no. 12, pp. 4062–4071, Dec. 2006.
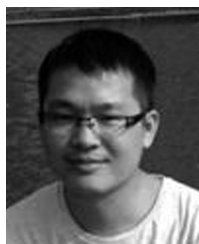
Zhicheng Lin (S'11) received the B.S. degree in physics from Lanzhou University, Lanzhou, China, in 2005, the M.S. degree in physics from South China Normal University, Guangzhou, China, in 2009, and currently is working toward the Ph.D. degree at the State-Key Laboratory of Analog and Mixed-Signal VLSI and FST-ECE, University of Macau, Macau, China.

His current research focuses on ULP radio front-ends and the RF circuit techniques for wideband software-defined-radio front-ends.

Pui-In Mak (S'00–M'08–SM'11) received the Ph.D. degree from the University of Macau (UM), Macao, China, in 2006.

He is currently an Associate Professor with the UM, and Coordinator of the Wireless and Biomedical Research Lines, State Key Laboratory of Analog and Mixed-Signal VLSI, UM. His group reported six state-of-the-art chips at ISSCC: wideband receivers (2011, 2014), micro-power amplifiers (2012, 2014), and ultra-low-power ZigBee receivers (2013, 2014).

He pioneered the world's first intelligent digital microfludic technology (iDMF) with nuclear magnetic resonance (NMR) and

polymerase chain reaction (PCR) capabilities. He authored *Analog-Baseband Architectures and Circuits for Multistandard and Low-Voltage Wireless Transceivers* (Springer, 2007) and *High-/Mixed-Voltage Analog and RF Circuit Techniques for Nanoscale CMOS* (Springer, 2012). His research interests are analog and RF circuits and systems for wireless, biomedical, and physical chemistry applications.

Dr. Mak has had numerous involvement with IEEE, including Distinguished Lecturer (2014–2015) and a member of the Board of Governors (2009–2011) of the IEEE Circuits and Systems Society (CASS); Editorial Board member of IEEE Press (2014–2016); senior editor of the IEEE Journal on Emerging and Selected Topics in Circuits and Systems (2014–2015); associate editor of the IEEE Transactions on Circuits and Systems–I, Regular Papers (2010–2011, 2014–present); associate editor of the IEEE Transactions on Circuits and Systems—II: Briefs (2010–2013); and guest editor of the IEEE RFIC Journal (2014). He is a Technical Program Committee (TPC) member of A-SSCC. He was the recipient of the IEEE DAC/ISSCC Student Paper Award (2005); the IEEE CASS Outstanding Young Author Award (2010); the National Scientific and Technological Progress Award (2011); and the Best Associate Editor for TCAS-II (2012–2013). In 2005, he was decorated with the Honorary Title of Value for scientific merits by the Macau Government.

Rui P. Martins (M'88–SM'99–F'08) was born April 30, 1957. He received the bachelor (five-year), masters, Ph.D., and Habilitation degrees for Full Professor in electrical engineering and computers from the Department of Electrical and Computer Engineering, Instituto Superior Técnico (IST), TU of Lisbon, Lisbon, Portugal, in 1980, 1985, 1992, and 2001, respectively.

Since October 1980, he has been with the Department of Electrical and Computer Engineering (DECE)/IST, TU of Lisbon. Since 1992, he has been on leave from IST, TU of Lisbon, and is also with the Faculty of Science and Technology (FST), Department of Electrical and Computer Engineering, University of Macau (UM), Macao, China, where he has been a Full Professor since 1998. With the FST, he was the Dean of the Faculty (1994–1997) and has been Vice-Rector of the UM since 1997. In September 2008, following the reform of the UM Charter, he was nominated after open international recruitment as Vice-Rector (Research) until August 2013. Within the scope of his teaching and research activities, he has taught 21 bachelor and master courses and has supervised (or cosupervised) 26 theses, Ph.D. (11), and masters (15). He created the Analog and Mixed-Signal VLSI Research Laboratory, UM, elevated in January 2011 to the State Key Lab of China (the first in engineering in Macao), and is its Founding Director. He has authored or coauthored 12 books, coauthored (5) and coedited (7), and 5 book chapters; 266 refereed papers in scientific journals (60) and in conference proceedings (206); as well as another 70 academic works for a total of 348 publications. He holds seven U.S. patents.

Prof. Martins was the founding chairman of the IEEE Macau Section (2003–2005) and of the IEEE Macau Joint Chapter on Circuits And Systems (CAS)/Communications (COM) (2005–2008) [2009 World Chapter of the Year of the IEEE Circuits And Systems Society (CASS)]. He was the general chair of the 2008 IEEE Asia–Pacific Conference on Circuits And Systems (APCCAS'2008) and was the vice president for Region 10 (Asia, Australia, and the Pacific) of the IEEE Circuits and Systems Society (CASS) (2009–2011). He was also currently the vice president (world) of regional activities and membership of the IEEE CAS Society (2012–2013). He is an associate editor for the IEEE Transactions on Circuits and Systems—II: Express Briefs (2010–2013). He is also a member of the IEEE CASS Fellow Evaluation Committee (Class of 2013). He was the recipient of two government decorations: the Medal of Professional Merit from the Macao Government (Portuguese Administration) (1999) and the Honorary Title of Value from Macao SAR Government (Chinese Administration) (2001). In July 2010, was elected unanimously as a corresponding member of the Portuguese Academy of Sciences, Lisbon, Portugal.